Structural, electronic and photochemical properties of cerium-doped zirconium titanate

Structural, electronic and photochemical properties of cerium-doped zirconium titanate

Valeria Polliotto[a], Elisa Albanese[b], Stefano Livraghi[a*], Stefano Agnoli[c], Gianfranco Pacchioni[b] and Elio Giamello[a]

a) Dipartimento di Chimica and NIS, Università di Torino, Via P. Giuria 7, 10125 Torino, Italy
b) Dipartimento di Scienza dei Materiali, Università Milano Bicocca, via R. Cozzi 55, 20125 Milano, Italy
c) Dipartimento di Chimica, Università di Padova, Via Via Marzolo 1, 35136 Padova, Italy

*stefano.livraghi@unito.it

Abstract

Mixed solid system involving cerium and zirconium titanate ($ZrTiO_4$) have been prepared using the sol-gel technique. Both X-ray diffraction and DFT calculations firmly indicate that, till a doping level of 10 mol%, cerium ions are dissolved in the titanate matrix (which has the scrutynite structure, analogous to those of the main TiO_2 polymorphs) occupying the cationic sites and progressively altering its cell parameters. Cerium is hosted in the matrix both in the form of Ce^{4+} and Ce^{3+} ions (XPS results). The trivalent state seems to be favoured even though the state of the dopant depends on the treatment undergone by the material. DFT calculations describe the intra band-gap states formed in both cases and the strong localisation of the single electron in the case of Ce^{3+} ($4f^1$). Differently from the case of Ce doped ZrO_2, that shows photoactivity in the visible light because of the presence of cerium, the doped titanate is inactive in the same conditions. Under UV-Vis illumination charge separation occurs (EPR results) and the low-loading doped systems (0.5%, 1%) form OH radicals, detected by spin trapping, more efficiently than the pristine matrix. The absence of photoactivity in the visible range is interpreted in terms of the detrimental role (charge recombination) played by both the occupied intra-band gap states associated to Ce^{3+} and the corresponding oxygen vacancies formed in the lattice by charge compensation.

Keywords: $ZrTiO_4$, cerium doping, EPR, DFT, XPS, photocatalysis

1. INTRODUCTION

The application of photoactive oxides in various technologies, such as photocatalysis,[1,2] solar energy conversion,[3,4] photoelectrochemical cells,[5,6] represents a research topic of paramount importance in order to face the energetic and environmental problems of the present age. Solid systems based on metal oxides have a major role in photocatalytic science and technologies since the experiment of photoassisted water electrolysis reported in 1972 performed employing a titanium dioxide film as a photoanode for water oxidation to molecular oxygen [7]. Since then, TiO_2 has been the reference system for environmental photocatalysis reactions in which the optimal oxidation potential of the holes, formed in the valence band (VB) upon photoexcitation with suitable photons, is exploited for the oxidative abatement of pollutants. A pioneering role in this particular area has been played by Ezio Pelizzetti[1,8] to whom the present volume is dedicated.

However, the application of the most important photoactive oxides, in many cases, is far from practical application because of either the rapid electron–hole recombination or the high value of band gap energies that limits the use of low frequency photons abundantly present in the solar light.[9] Among the possible strategies to overcome these drawbacks,[10] the modification of photoactive oxides with different kinds of dopants has been pursued using both metal and nonmetal elements.[11,12] Doping the structure of an oxide with Ce ions or, in the case of non-solubility of the two components, supporting Cerium dioxide on the oxide matrix, represents a recently investigated topic in order to extend the intrinsic photoactivity of these solids to the visible region of the solar spectrum.[13-17]

Insertion of Ce^{4+} cations into the lattice of several oxides, such as TiO_2, is a questioned point in the literature. Insertion of Ce ions in titania is usually limited to the case of low dopant loading range,[18-20] even though with some exception.[21] This limitation is understandable if the strong structural difference between cerium oxide (fluoritic structure) and the polymorphs of TiO_2 (all

based on linked octahedra) is considered. Moving to higher Ce loading, in fact, leads to phase segregation and formation of heterojunctions between the two oxides.[22-24] In this second case, at the interface, small domains of a mixed phases of cerium titanate ($Ce_2Ti_2O_7$, pyrochlore structure) can be also formed depending on the procedure followed for the preparation of the mixed materials. The presence of $Ce_2Ti_2O_7$ induces a red shift of the absorption edge with respect to the pure oxides, which causes an absorption in the visible range. This is due to the presence of Ce^{3+} (that has partially populated 4f levels) in the titanate that absorbs in the visible spectrum.[22] For this reason, mixed Ti-Ce oxide materials were tested in the photodegradation of a variety of model pollutants, such as Rhodamine B120 and formaldehyde.[25,26] The formation of a heterojunction for instance, is also at the base of the visible light activity of ZnO-CeO_2 mixed oxide.[27]

Differently from the previous cases, solid solutions of Ce ions in the ZrO_2 lattice can be easily formed due to the structural analogy of CeO_2 and ZrO_2 and to the lower difference of the ionic radii of the Ce^{4+} - Zr^{4+} pair with respect to the Ce^{4+} - Ti^{4+} one. Ce doped zirconium dioxide systems were deeply investigated in the past for their improved mechanical and electrical properties.[28] Even though ZrO_2 is characterized by a large band gap value (E_g> 5eV), it has recently been reported that the dispersion of small amounts of cerium ions in the ZrO_2 lattice makes it photosensitive to visible light, according to the model designed by N. Serpone and A. Emeline where they forecast the nature of the photocatalysts of third generation.[29-31] This photosensitivity has been ascribed to intra-band gap Ce 4f empty states, which should act as a bridge between the valence band and the conduction band of the oxide, allowing low-energy photons to excite electrons from one band to the other.[32-34]

In the present paper we turn our attention to the effect of Ce doping in zirconium titanate ($ZrTiO_4$). Zirconium titanate is a material widely used in several technological applications.[35-38]. Zirconium titanate, $ZrTiO_4$ and $ZrTi_2O_6$ or srilankite, are the only stable ternary compounds in the ZrO_2-TiO_2

phase diagram. They both have an interesting peculiarity since their structure (orthorhombic Pbcn) is alike to those of all TiO_2 polymorphs, being based on TiO_6 octahedra linked by three-fold coordinated oxygen ions. In the structure of $ZrTiO_4$, both titanium and zirconium ions are randomly distributed on equivalent octahedral sites and are surrounded by six oxygen atoms and the oxygen atoms are connected to three metals ions.[39] From the point of view of the optical properties this material shows a band gap value (~3.8eV) between that of the two parent oxides (ZrO_2, TiO_2), and charge carriers separation can be induced by UV light absorption making this material a possible candidate for photochemical applications.[40] Moreover, sensitization to the visible component of the electromagnetic spectrum can be achieved by band gap engineering.[41] In analogy to what observed with the CeO_2-ZrO_2 system, the solubility of cerium in this matrix should be hampered by the strong structural difference. However, as it will be shown and discussed in the following, a series of samples with excellent solubility of cerium ions in the $ZrTiO_4$ matrix till a value of 10% molar percentage has been obtained.

The cerium doped materials have been investigated pointing to their photochemical properties in two distinct ranges of frequencies (visible light and UV-Vis). Their properties have been constantly compared with those of the pristine zirconium titanate (band gap value of ~3.8 eV). In particular, the charge separation under illumination has been followed by Electron Paramagnetic Resonance (EPR) and the formation of Reactive Oxygen Species (ROS) either by spectrophotometry (superoxide radicals) or by spin trapping (OH radicals). The experimental results are coupled with a thorough theoretical investigation of the mixed material performed using state of the art DFT approaches in order to elucidate the electronic structure of the system with particular attention to the modifications occurring in the band gap region caused by the presence of cerium ions.

2. EXPERIMENTAL

2.1. Samples preparation

The pristine $ZrTiO_4$ powder (hereafter ZT) was prepared via the sol−gel technique, mixing a solution of 3.5 ml of titanium(IV) isopropoxide and 5 ml of zirconium(IV) propoxide (molar ratio 1:1) in 9 ml of 2-propanol and adding 3.5 ml of water. The gel was left to age for 15 hours at 290 K and subsequently dried at 343 K. The dried material was calcined in air at 973 K for 1 hour. The powder presented a white color. Ce doped-$ZrTiO_4$ powders (hereafter Cex-ZT where x is the Ce molar ratio) powders were prepared in a similar manner, mixing a solution of 3.5 ml of titanium(IV) isopropoxide and 5 ml of zirconium(IV) propoxide (molar ratio 1:1) in 9 ml of 2-propanol to which 3.5 ml of water solution of $CeCl_3 \cdot 7H_2O$ was added in order to have different molar ratio of cerium (from 0.5 mol% to 10 mol%, Table 1). The gel was left to age for 15 hours at 290 K and subsequently dried at 343 K. The dried materials were calcined in air at 973 K for 1 hour. The powder presented yellow color, more vivid in the case of the Ce10-ZT sample.

2.2. Characterization

The elemental analysis was performed by means of X-ray fluorescence (XRF) spectroscopy. The samples were analyzed using an EDAX Eagle III energy-dispersive micro-XRF (μXRF) spectrometer equipped with a Rh X-ray tube. Powder X-ray diffraction (XRD) patterns were recorded with a PANalytical PW3040/60 X'Pert PRO MPD diffractometer using a copper Kα radiation source (0.154056 nm). The intensities were obtained in the 2θ range between 20° and 80°. X'Pert High-Score software was used for data handling. Diffraction patterns were refined with Rietveld method using MAUD (Material Analysis Using Diffraction) program.[42,43]

UV-Visible absorption spectra were recorded using a Varian Cary 5 spectrometer, coupled with an integration sphere for diffuse reflectance studies, using a Carywin-UV/scan software. A sample of PTFE with 100% reflectance was used as the reference. Spectra were registered in the 200–800 nm range at a scan rate of 240 nm/min with a step size of 1 nm. The measured intensities were converted with the Kubelka-Munk function.

The surface area measurement was carried out on a Micromeritics ASAP 2020/2010 apparatus using the Brunauer–Emmett–Teller (BET) model for N_2 adsorption measurements. Prior to the adsorption run, the sample was outgassed at 573 K for 2 hours.

Continuous Wave Electron Paramagnetic Resonance (CW-EPR) experiments were performed with a Bruker EMX spectrometer operating at X-band (9.5 GHz), equipped with a cylindrical cavity operating at 100 kHz field modulation. All the spectra were recorded with a Modulation Amplitude of 0.2 mT. Spectra under irradiation were recorded “in situ”, directly illuminating the sample, kept at 77 K in liquid nitrogen, inside the EPR cavity using a 1600 W Newport Xe lamp.

For the X-ray photoemission spectroscopy (XPS) measurements, the oxide powers were suspended in MilliQ water, sonicated for 15 minutes and drop casted on gold coated aluminum supports. The resulting thin film samples were introduced into the load lock of an ultra-high vacuum system and left outgassing overnight at a base pressure better than $5x10^{-7}$ mbar. Then photoemission measurements were taken in the main chamber of the ultra-high vacuum system at a base pressure of $5x10^{-9}$ mbar at room temperature, by using an Omicron DAR 400 x-ray source (Al Kα=1486.7 eV) and a VG Mk II Escalab electron analyzer.

Due to the semiconducting nature of the powders, a homogeneous charging was observed, therefore the binding energy (BE) scale was adjusted using the adventitious carbon signal and setting its position to 284.8 eV. After the photoemission measurements, the samples were subjected to an oxygen treatment in a near ambient pressure cell directly connected to the spectrometer, without any air exposure. The samples were annealed at 400°C in 5 mbar O_2 (purity 5.0) for 30 minutes and then transferred back to the analysis chamber for further measurements, under ultra-high vacuum conditions. The photoemission lines were analyzed using the XPSPEAK 4.1 software, which uses a mixed linear and Shirley background, and symmetrical Gaussian-Lorentzian product functions.

2.3. Reactive Oxygen Species (ROS) detection

The photocatalytic production of the superoxide ion ($O_2^{\bullet-}$) in water solution was followed via spectrophotometry using a specific reaction of the species with nitroblue tetrazolium (NBT). This molecule can be reduced by the superoxide ion ($O_2^{\bullet-}$) forming the insoluble purple formazan ($NBTH_2$). Although formazan is soluble in aprotic solvents, it is insoluble in aqueous solutions. Hence, when formazan is produced during photocatalytic reactions in aqueous solutions a precipitation occurs. The amount of photogenerated superoxide ions was detected measuring the intensity decrease of the absorption maximum at 259 nm of NBT in the solution.

The tests were performed with 50 ml of NBT (20 μM) water solution and 0.05 g of photocatalyst powder (concentration of 1 g/l of photocatalyst). The suspension was left in dark for 15 minutes before irradiation with UV-Visible light. Every 15 minutes of irradiation 3 ml of suspension was taken and the powder was removed from the solution by centrifugation. The supernatant solution was placed into a quartz cell in order to record the UV-Visible absorption spectra. The monitored process can be described by the reactions reported below:

$ZrTiO_4 + h\nu \longrightarrow e^-_{(CB)} + h^+_{(VB)}$ (1)

$O_2 + e^- \longrightarrow O_2^{\bullet-}$ (2)

$4O_2^{\bullet-} + NBT^{2+} + 2H^+ \rightarrow TBNH_2 + 4O_2.$ (3)

The formation and reactivity of holes upon irradiation was tested monitoring the formation of hydroxyl radicals ($OH^\bullet$) in aqueous solution. $OH^\bullet$ radicals are formed by the reaction between water and the photo-generated holes according to the following equations:

$h^+ + H_2O \longrightarrow OH^\bullet + H^+$ (4)

Due to their high reactivity, $OH^\bullet$ radicals can be detected by EPR in solution only using a spin trap molecule namely 5,5-dimethyl-pyrroline N-oxide (DMPO), a diamagnetic molecule that, reacting with $OH^\bullet$ radicals, forms a relatively stable radical detectable with EPR spectroscopy (reaction 5).

$OH^{\bullet}$ + DMPO → DMPO-$OH^{\bullet}$ (5)

For these tests, 500 µl of phosphate buffer 0.5 M and 250 µl of water were added to 250 µl of DMPO 0.085M water solution. 27 mg of the photocatalyst powder were added to the solution. The suspension was irradiated with UV-Visible light (excluding the deep UV components with a cut-off at 315 nm) with an irradiance of 200 W/m^2. At different irradiation time the EPR spectra of the solution were recorded collecting the sample with a capillary. For both the tests ($O_2^{\bullet-}$ and $OH^{\bullet}$), the samples were irradiated with UV-vis light using a 500 W Xe-Hg lamp equipped with a IR water filter.

2.4. DFT calculations

The DFT hybrid functional B3LYP [44,45] as implemented in CRYSTAL14 [46] has been adopted for all the calculations. An all electron basis set was used for O (8-411(d1)), N (7-311(d1)) and Ti (86-411(d41)). For Zr, a 311(d1) basis set associated to an effective core potential (Hay and Wadt small-core ECP) has been adopted.[47] Also for Ce an ECP has been used,[48] and the electrons explicitly treated are $4s^2 4p^6 4d^{10} 5s^2 5p^6 4f^1 6s^2 5d^1$, with a (10sp7d8f)/[4sp2d3f] basis set properly optimized.[49]

The computed optimal lattice parameters for $ZrTiO_4$ are a = 4.860 Å, b = 5.515 Å, c = 5.078 Å. A 2x2x1 supercell containing 48 atoms was used to represent the crystal. This corresponds to a dopant percentage of 6.25% with respect to all the metal ions and of 12.5% with respect to Zr (or Ti) ions. In the case of Ce^{3+}-$ZrTiO_4$-V_O, where V_O is an oxygen vacancy, and Ce substitutional in the $ZrTiO_4$ surface, a 2x2x2 supercell has been adopted. The accuracy of the integral calculations was increased to 7, 7, 7, 7 and 14.

3. RESULTS and DISCUSSION

3.1. Structural and optical properties

The specific surface area of the samples was measured by N_2 physisorption (B.E.T) and the values are reported in Table 1. The samples exhibit specific surface area in a range roughly between 50 m^2/g and 70 m^2/g. The insertion of variable amounts of Ce in the ZT matrix, thus, slightly affects the specific surface area of the samples. XRD patterns of the Ce doped-$ZrTiO_4$ powders, compared with that of pristine $ZrTiO_4$ (ZT) are reported in Figures 1 and 2. Data in Figure 1 show that for the three low-loading samples (0.5-1 mol%) only the $ZrTiO_4$ phase (Scrutinyte structure) is present, while for two samples with higher cerium loading a minor fraction of the tetragonal ZrO_2 phase is also observed (about 5%). It is worth noting that no segregation of cerium oxide is observed for the whole set of Ce- doped samples. This, in principle, suggests that cerium ions are able to enter in the $ZrTiO_4$ lattice forming a solid solution. However, considering that Ce easily forms solid solution with ZrO_2, also the presence of substitutional cerium ions in this minority component of the system cannot be excluded.[28,50]

Sample	Ce loading (mol%)	$ZrTiO_4$ (%w/w)	ZrO_2 (%w/w)	Cristallites $ZrTiO_4$ (nm)	Cristallites ZrO_2 (nm)	R(%)	BET (m^2/g)	BG (eV)
ZT	-	100	-	23±0.2	-	5.7	62	3.8
Ce05-ZT	05	100	-	20±0.2	-	5.4	61	3.8
Ce08-ZT	08	100	-	23±0.1	-	6.2	51	3.8
Ce1-ZT	1	100	-	19±0.2	-	5.5	61	3.8
Ce8-ZT	8	95	5	27±0.2	22±4.0	6.1	50	3.7
Ce10-ZT	10	95	5	18±2.3	16±2.6	5.8	72	3.7

Table 1: Phase composition, crystallites size of the pristine and Ce doped $ZrTiO_4$ samples evaluated via Rietveld refinement of the XRD patterns reported in Figure 1 and the corresponding specific surface area and Band Gap edge evaluated by Tauc plot.

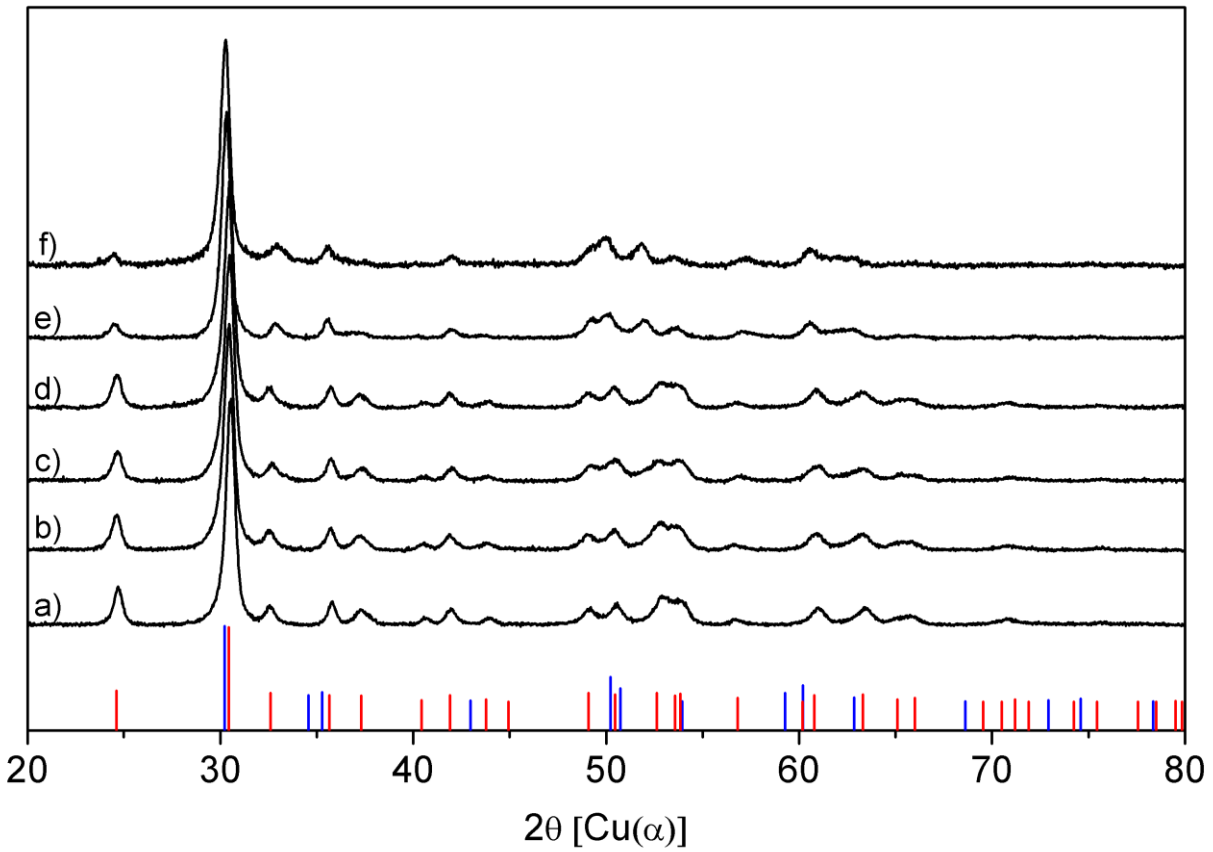

Figure 1: XRD patterns of pristine $ZrTiO_4$ (a) and Ce doped $ZrTiO_4$ samples 0.5 mol% (b), 0.8 mol% (c), 1 mol% (d), 8 mol% (e), and 10 mol% (f). In the lower part the reference patterns for $ZrTiO_4$ (ICSD 00-034-0415, red sticks) and ZrO_2 (ICSD 01-079-1766, blue sticks) are reported.

A second, convincing evidence of the formation of a solid solution between Cerium and $ZrTiO_4$ is the progressive change of the lattice parameters obtained by a Rietveld refinement of the XRD patterns of the materials containing different amounts of cerium (Figure 2 and table 2). In Figure 2A the magnification of the first three diffraction peaks is reported to better appreciate their continuous shift with respect to the pristine material, which is proportional to Ce loading. Figure 2B shows the lattice parameters deviation from that of the pure $ZrTiO_4$ sample. This applies particularly to the lattice parameters a and b that are more affected than c by Ce insertion.

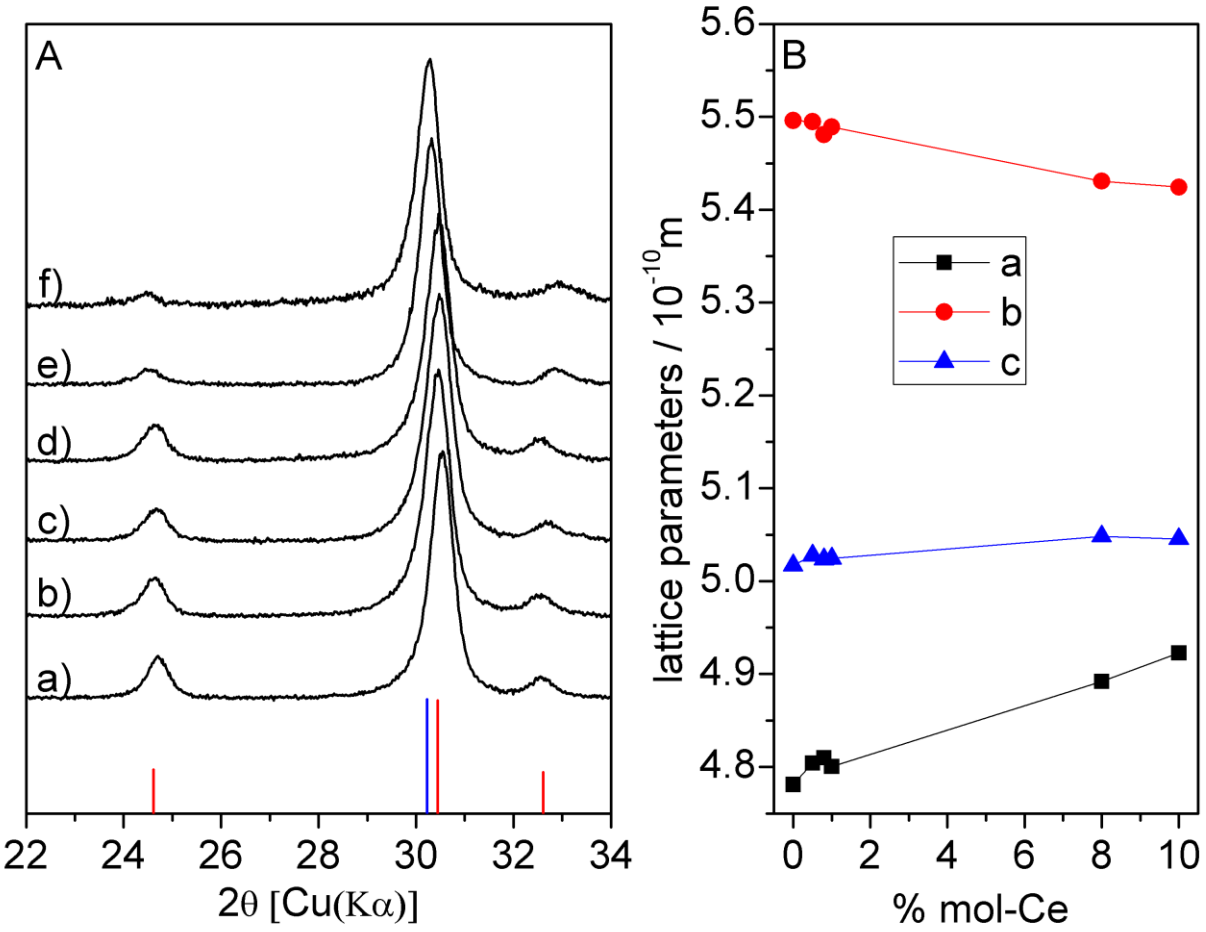

Figure 2: Panel A: magnification of the first three XRD diffraction peaks of the data of Figure 1. Pristine $ZrTiO_4$ (a) and Ce doped $ZrTiO_4$ samples respectively with 0.5 mol% (b), 0.8 mol% (c), 1 mol% (d), 8 mol% (e), 10 mol% (f). In the lower part of the reference patterns for $ZrTiO_4$ (ICSD 00-034-0415, red sticks) and ZrO_2 (ICSD 01-079-1766, blue sticks). Panel B: Lattice parameters obtained from Rietveld refinement of the XRD patterns of differently loaded samples.

The change of the lattice parameter as a consequence of the Ce insertion in the $ZrTiO_4$ lattice is also confirmed by theoretical calculations (see section 3.2). In the structure of $ZrTiO_4$ a dopant percentage of 6.25% with respect to all metal ions and of 12.5% with respect to Zr ions has been considered. In this model the Ce atoms were inserted either as substitutional to one Zr atom (Ce_{subZr}-$ZrTiO_4$) or to one Ti atom (Ce_{subTi}-$ZrTiO_4$). The differences (expressed in %) of the computed cell parameters with respect to that calculated for pure $ZrTiO_4$ are reported in table 2 and are compared with the corresponding experimental values. The calculated values are in good agreement with the trend obtained for the experimental ones.

To summarize, XRD characterization and DFT calculations converge in providing evidence about the insertion of Ce in the lattice of zirconium titanate. The $ZrTiO_4$ matrix therefore, from the point of view of the affinity for the Ce ions, shows the same behavior of ZrO_2 (solubility) rather than that of TiO_2 (poly-phasic systems).

	ZT	Ce0.5-ZT	Ce0.8-ZT	Ce1-ZT	Ce8-ZT	Ce10-ZT
a [Å]	4,7812	4,8042	4,8099	4,8005	4,8919	4,9227
b [Å]	5,4959	5,4948	5,4808	5,4888	5,4307	5,4243
c [Å]	5,0171	5,0194	5,0236	5,0246	5,0484	5,0457

	Expt					Calc (Ce6.25)	
	Ce0.5	**Ce0.8**	**Ce1**	**Ce8**	**Ce10**	**Ce_{subZr}**	**Ce_{subTi}**
Δ%a	0,48	0,60	0,40	2,32	2,96	1.13	1.66
Δ%b	-0,02	-0,27	-0,13	-1,19	-1,30	-0.38	-0.26
Δ%c	0,05	0,13	0,15	0,62	0,57	0.11	0.88

Table 2: Upper part, lattice parameters (Å) obtained from Rietveld refinement of sample with different percentages of cerium. Bottom Expt: Measured cell parameters difference (Δ= Ce-ZT–ZT) of cerium doped materials compared to pristine zirconium titanate (expressed in %). Calc: Calculated cell parameter difference for a given cerium composition with respect to calculated pristine $ZrTiO_4$.

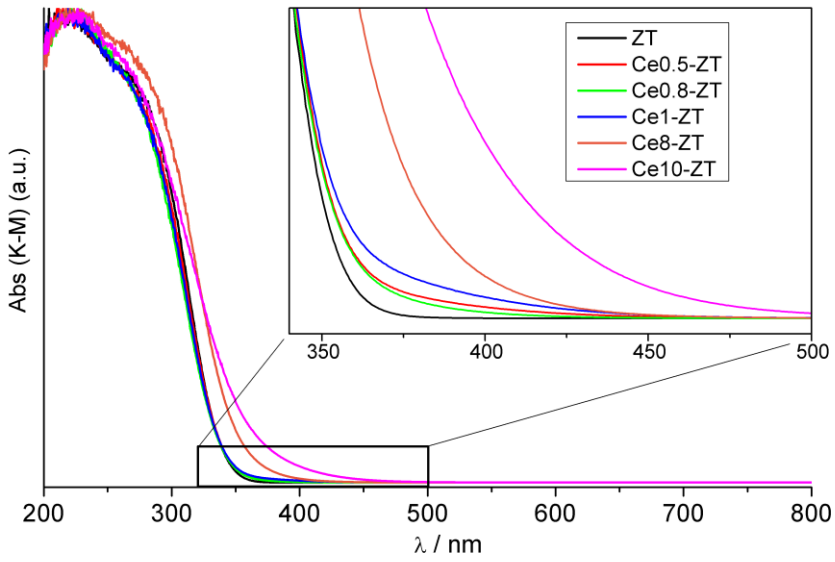

Figure 3: UV-Visible Diffuse Reflectance Spectra of Ce-ZT powders.

The optical absorption spectra in the UV and visible region of various Ce-ZT materials are shown in Figure 3 and the optical band gap energy evaluated by the Tauc's plot method (see S.I., Figure S3) for a direct transition of the Ce-ZT samples are listed in Table 1. For low amount of Ce (from 0.5% to 1%) the UV-Visible spectra differs from that of bare ZT sample only for a tail from 350 nm to 450 nm that lends a light yellow color of the powders. For higher loading (8%-10%), the absorption tail described above is associated to a small but appreciable red shift of the band gap with respect to the bare $ZrTiO_4$. In all samples the energy edge of the transition between valence band and conduction band remains in the UV region and the origin of the yellow color of the solid is the tail in the visible region.

The valence state of cerium ions has been investigated by X-ray photoelectron spectroscopy. Figure 4 shows the XPS data for the two limiting values of the compositional range (Ce0.5-ZT and Ce10-ZT samples). XPS data indicate that the stoichiometry of the precursors is substantially transferred to the final materials, suggesting that the cerium distribution between surface and bulk is homogeneous (see S.I.). Surprisingly, for both samples XPS measurements indicate that an important fraction of Ce ions is present in the reduced form of Ce^{3+} species.

The Ce 3d photoemission spectra for the Ce05-ZT and Ce10-ZT samples are reported in Figure 4. According to the classic nomenclature by Burrows et al.,[51] the photoemission line comprises five distinct doublets corresponding to the $3d_{5/2}$ (v-labelled) and $3d_{3/2}$ (u-labelled) levels, three of which pertain to Ce^{4+} and two to Ce^{3+}. This complexity is due to the mixed valent ground state of Ce(IV) ions[52] that can be described as a mixture of $4f^0$ (v'''/u''') $4f^1L^{-1}$ (v/u) and $4f^2L^{-2}$ (v"/u") (where L^{-1} and L^{-2} indicate one or two holes in the ligand, i.e. oxygen 2p levels, respectively). Similarly, the Ce^{3+} ions exhibit two possible ground state configurations namely $4f^1$ (v') and $4f^1L^{-1}(v^0)$. In order to determine the ratio between Ce^{3+} and Ce^{4+} species, we carried out a multipeak analysis using symmetrical Gaussian-Lorentzian product functions, whose main parameters (i.e. full with at half

maximum, BE energy position etc.) have been previously identified using proper standards (i.e. stoichiometric CeO_2 powder and Ce(III) nitrate) and applied with only minor adjustments. The results are in good agreement with previous literature data.[53,54]

In both the Ce0.5-ZT and Ce10-ZT samples, a relevant amount of Ce^{3+} species is present: 47.9% and 42%, respectively. On the other hand, on the Zr 3d and Ti 2p core level spectra no significant reduced components can be observed.

This strong stabilization of Ceria in a reduced oxidation state is in excellent agreement with previous theoretical[55] and experimental works,[53,56] which indicate that in the composites between ceria and other reducible oxides as for example TiO_2, there is the possibility of an easy electron transfer from the Ti 3d to the Ce 4f levels that therefore act as actual electron sinks and result to be populated by an unusually high amount of electrons.

Interestingly, in these oxide solid solutions, the Ce^{3+}/Ce^{4+} redox couple results to be extremely reversible. As a matter of fact, in the case of the Ce10-ZT sample, after annealing for 30 minutes under ultra-high vacuum conditions at 500°C, the fraction of Ce^{3+} species increases to 83.7%, whereas, if the annealing is carried out in oxidative conditions (400°C in 5 mbar of pure O_2), the amount of Ce^{3+} drops to 24.9%. Whereas the changes in the Ce3d levels are quite apparent, only negligible changes are observed in the Zr 3d and Ti 2p core level levels, indicating that the redox chemistry of the materials is mostly controlled by the cerium species although they are present in smaller amount.

Even though a fraction of the observed Ce^{3+} could be the consequence of the unavoidable reduction occurring in ultra-high vacuum during the XPS measurement, the oxidation experiments (see experimental details) clearly show that Ce^{3+} is not stable and the cerium can be further, though not completely oxidized. Our view of the investigated system, taking into account the well-known redox sensitivity of cerium ions, is that of a solid containing both trivalent and tetravalent cerium ions

whose quantitative ratio is variable and markedly dependent on both the temperature and the atmosphere composition. However, it cannot be excluded that, in the present case, the choice of $CeCl_3$ for the synthesis could have partially favored the presence of trivalent cerium in the final calcined solid.

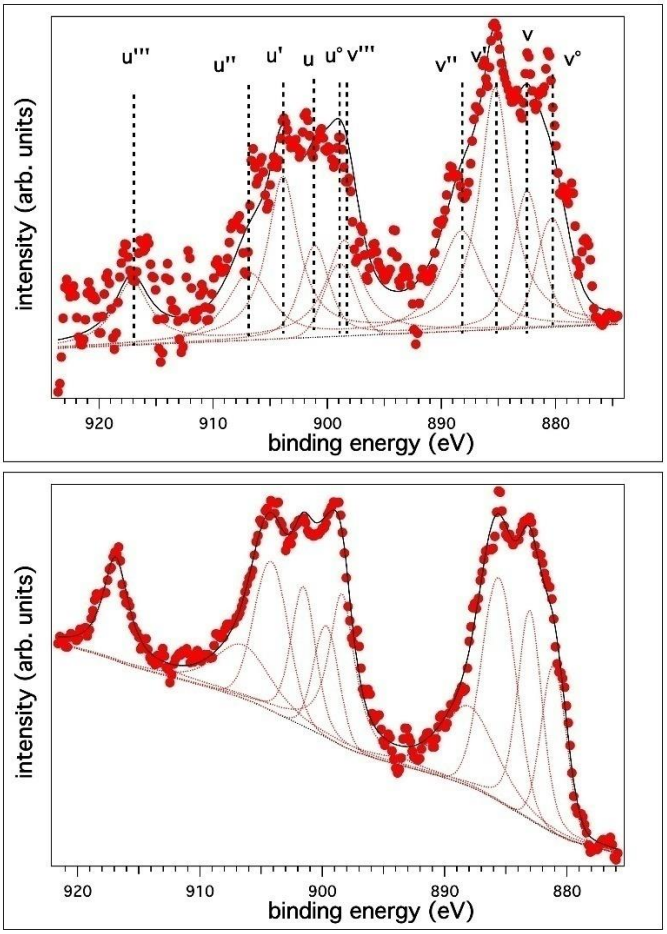

Figure 4: XPS data of Ce0.5-ZT (upper panel) and Ce10-ZT (lower panel) powders.

3.2. Electronic structure from DFT calculations

Ce^{4+}-doped $ZrTiO_4$

In order to obtain a more accurate description of Ce modified zirconium titanate and to understand the origin of the optical absorption, the band structure of a Ce-$ZrTiO_4$ (6.25% doping) has been computed. We have seen already that the DFT calculated lattice parameters support the view of Ce^{4+} ions that replace the original cations at lattice positions (see previous Section 3.1). This result is in line with the finding that, as in the case of ZrO_2, a solid solution of Ce ions in $ZrTiO_4$ is formed.

We also checked the preferential presence of Ce^{4+} dopants in the bulk or at the surface of $ZrTiO_4$. To this end, a model of a (010) $ZrTiO_4$ has been constructed, and the dependence of the surface energy has been studied as a function of the number of layers in the slab model (See Supporting Information, Fig. S1 and Table S1). Then, Ti and Zr ions at the surface of in the inner layers of the slabs have been replaced by Ce, finding that surface doping is always preferred to bulk doping (see Fig. S2 and Table S2). This is consistent with the lattice expansion associated to the substitutional doping.

As already mentioned, the Ce atoms were inserted both as substitutional to Zr ($Ce_{sub}Zr$-$ZrTiO_4$) or substitutional to Ti ($Ce_{sub}Ti$-$ZrTiO_4$). In both cases, the 4f empty states of Ce lie very high in energy, about 0.5 eV below the conduction band, in the energy range of 4.1-4.4 eV (see Figure 5 where both bands and density of states are reported). E_g computed for $ZrTiO_4$ with the present method, 4.72 eV, is much larger than that measured experimentally. The problem has been analyzed in detail in ref. 38 and the reader is referred to this paper for a more throughout discussion. The large $ZrTiO_4$ band gap is related to the Ti component. The absolute values are too large due to the fact that the B3LYP functional tends, in the case of TiO_2, to overestimate the band gap (by about 21%). Applying this correction, the empty 4f states are expected a much lower energies, around 3.2-3.5 eV, similar to what found for the Ce-ZrO_2 system.[31]

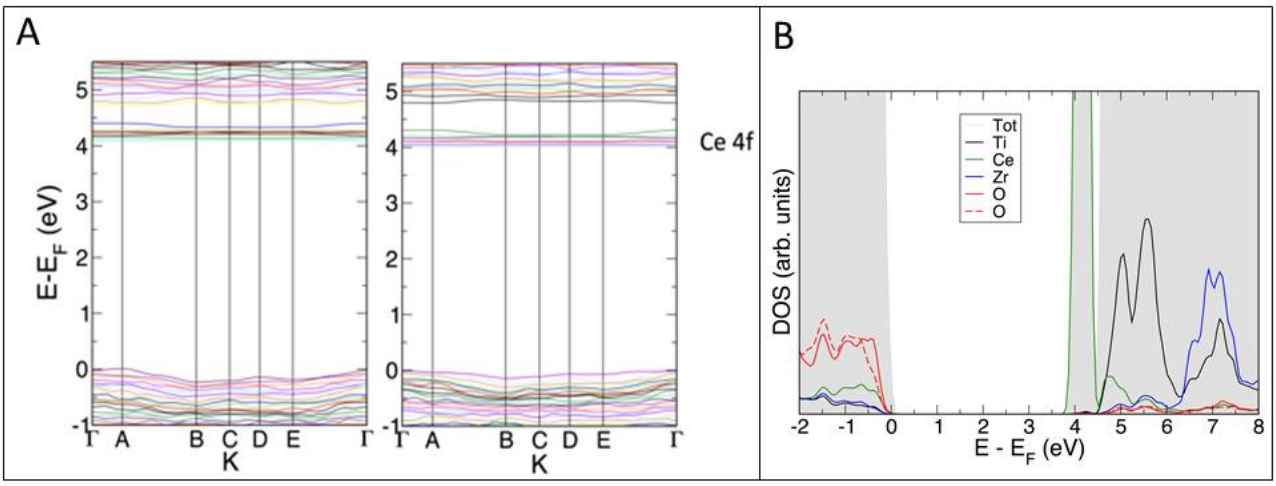

Figure 5: Panel A: Band structures of the Ce_{subZr}-$ZrTiO_4$ (left) and Ce_{subTi}-$ZrTiO_4$ (right) crystals. Panel B: TDOS and PDOS of Ce_{subZr}-$ZrTiO_4$ structure.

The analysis of the density of states as derived from the Kohn-Sham energy levels is thus not able to explain the optical absorption tail in the visible range. However, Kohn-Sham energy levels provide only a crude approximation to the band gap excitation. Hence, in order to obtain a more rigorous description of the band structure when electronic transitions are involved, the calculation of transition energy levels between different charge states for a defective system has been performed using the Charge Transition Levels (CTL) method.[57] The CTLs can be derived on the basis of Janak's theorem.[58] Through this method it is possible to calculate with more accuracy the position of the defect levels generated by the optical excitation from the VB of the material and thus, in this case, the energy related to the transformation of a mid-gap Ce^{4+} ion to Ce^{3+}. The transition level ε[(q+1)/q] is defined as the Fermi level for which the formation energies of defects in the charge states q+1 (in this case Ce^{4+}) and q(Ce^{3+}) are equal. For Ce_{sub}Zr-$ZrTiO_4$ (Figure 6) this transition, that involves the excitation of one electron from the VB to a Ce ion, occurs at 2.32 eV. This excitation is now in agreement with the experimental observed absorption in the visible range of the Ce doped materials.

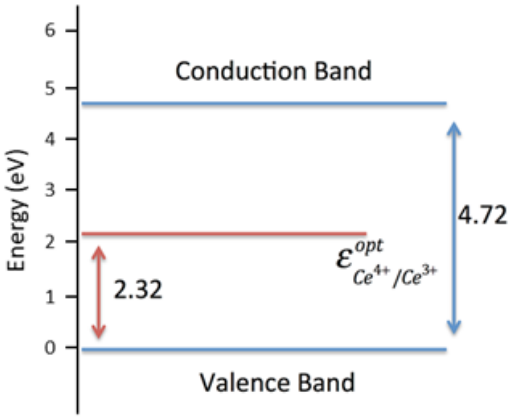

Figure 6: Optical transition levels for ZrTiO4 systems doped with a single Ce atom. The position of Ce^{3+} states is reported.

Interestingly, in spite of the energy difference between the Ce 4f states in Ce-ZrO_2 and Ce-$ZrTiO_4$ (3.2 eV with respect to 4.1 eV, respectively), the optical transition level ε_{opt}, 2.5 eV for the Ce-ZrO_2 (tetragonal polymorph), and 2.3 eV for Ce-$ZrTiO_4$, is similar.[31] Consequently, the two doped oxides differ only in terms of separation between the Ce-related mid-gap states and the conduction band of the oxide (3.2 eV and 2.4 eV, respectively), much higher for the Ce-doped ZrO_2 than for Ce-$ZrTiO_4$.

Ce^{3+}-doped $ZrTiO_4$

Since the XPS characterization pointed out the relevant presence of Ce^{3+} ions in the samples, the simulation of Ce^{3+} ions in the structure of $ZrTiO_4$ has been also considered (Figure 7). To ensure the neutrality of the system, two Ce^{3+} ions and one oxygen vacancy (V_O) have been introduced in the lattice. An O vacancy in fact releases two excess electrons that can be stabilized on the mid-gap Ce 4f states. The two Ce have been inserted one as substitutional to Zr and the second one substitutional to Ti.

Indeed, after structure optimization, the two excess electrons generated by the V_O are fully localized on the two Ce ions that, therefore, are reduced from Ce^{4+} to Ce^{3+} (see spin density plot in the inset of Figure 7). Thus, we attribute the large number of Ce^{3+} ions present in the material (see analysis

of the XPS spectra above) to the partial loss of oxygen which is responsible for the formation of the reduced Ce ions.

In Figure 7, the electronic band structure is reported. Accordingly, the two semi-occupied 4f states of Ce^{3+} ions are very flat, sign of absence of dispersion and complete localization, and lie in the middle of the band gap at about 2.4-2.5 eV above the valence band. According to this Kohn-Sham energy levels, visible light could promote electronic transitions from the localized Ce^{3+} states to the conduction. Thus, also Ce^{3+} ions can contribute to the visible light absorption of Ce-doped $ZrTiO_4$ samples.

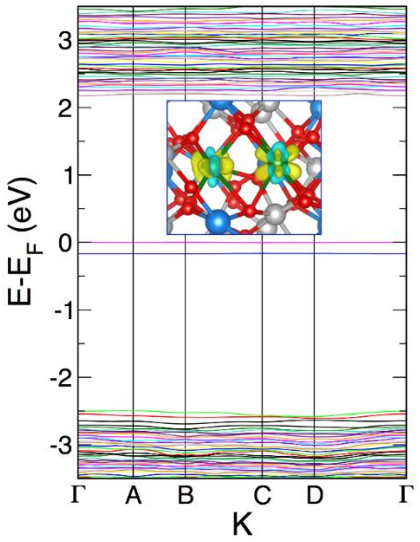

Figure 7: Band structure of $2Ce^{3+}$-$ZrTiO_4$-VO relaxed structure. In the inset the spin density (isosurface threshold values 0.007 e/a.u.3).

3.3. Photo-generation and reactivity of charge carriers followed by EPR

Since the optical absorption spectra of Ce-ZT samples (Figure 3) show absorptions ranging from the UV to the visible wavelengths, the effects of irradiation with both visible and UV-Visible light have been followed by EPR. The essential step of all photochemical applications is the charge spatial separation occurring in a photoactive material induced by photons of suitable energy. This entails

the promotion of electrons (e^-) in the conduction band (CB) and the formation of holes (h^+) in the valence band (VB) as described by the equation 1.[40]

The so photogenerated electrons and holes, in turn, can be trapped by lattice cations or lattice oxygen anions respectively, giving rise to paramagnetic species detectable via EPR. In pure $ZrTiO_4$ these are respectively Ti^{3+}/Zr^{3+} in the case of the electrons, and $O^{\bullet-}$ in the case of holes, according to the processes listed below.[40]

$$e^-_{(CB)} + Ti^{4+}/Zr^{4+} \rightarrow Ti^{3+}/Zr^{3+} \quad (6)$$

$$h^+_{(VB)} + O^{2-} \rightarrow O^{\bullet-} \quad (7)$$

In spite of the (weak) optical absorption occurring in the visible region, for all samples, the irradiation in this range (cut-off 400 nm) does not cause any significant change in the EPR spectra indicating that a charge separation in this conditions does not occur (data not reported for sake of brevity).

On the other hand, as in the case of bare ZT sample, the irradiation with UV-Visible of Ce-ZT samples causes a charge carrier separation in the material. Figure 8 reports the EPR spectra of Ce05-ZT irradiated with UV-Visible polychromatic light. The spectrum of the sample under vacuum in dark (Figure 8a) exhibits the same feature of that of the pristine ZT sample, i.e. it contains a tiny amount of Zr^{3+} ions already before irradiation.[40] It is useful here to remind that Ce^{3+} ions that are present in the material as indicated by XPS, are paramagnetic, but undetectable by EPR in our experimental conditions.[31] Upon UV-Visible irradiation (Figure 8b) on the right-hand side of the spectrum the signal of Zr^{3+} increases and simultaneously a week and very broad signal due to Ti^{3+} appears, indicating the trapping of photoexcited electrons. In parallel, at lower field a signal belonging to trapped holes ($O^{\bullet-}$ ions) clearly growths.

By heating the sample at room temperature, holes and electrons recombine, and the spectrum (recorded at 77K, Figure 8c) recovers the features observed before irradiation. This behaviour exactly reproduces that of pristine ZT sample.

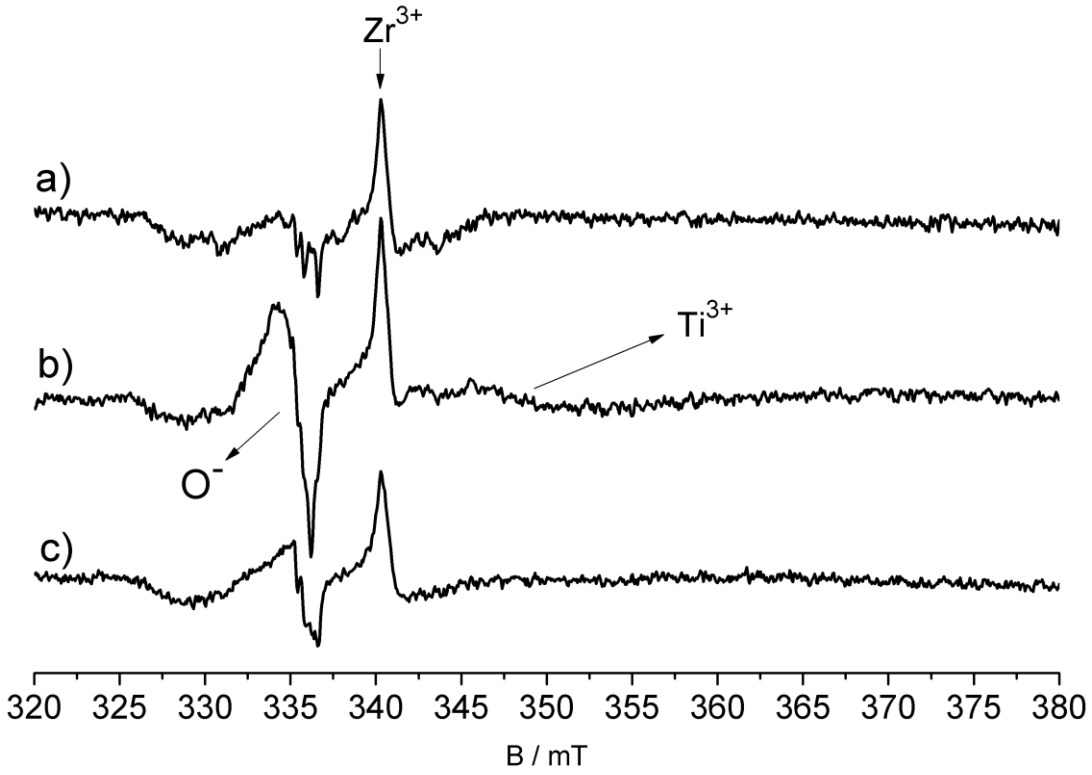

Figure 8: EPR spectra showing the effect of UV−Visible irradiation of Ce0.5-ZT in vacuum: (a) sample in the dark; (b) after UV−Visible irradiation; (c) sample after a thaw−freeze treatment (lamp off, heating at RT and cooling again at 77 K). All the spectra were recorded at 77 K and with a microwave power of 10 mW.

As detailed in the Experimental section, the surface reactivity of photogenerated charge carriers can be monitored by means of EPR. In order to evaluate their photoactivity, two tests on both pristine and Ce-doped ZT materials (ZT and Ce-ZT samples) were performed in solution, monitoring the formation of two different types of reactive oxygen reactive species (ROS) that are essential intermediates in photocatalytic applications.[59] To test the reductive ability of the solids, the superoxide formation in solution has been monitored measuring the drop of the optical absorption of nitroblue tetrazolium (NBT) by spectrophotometry (Fig. 9A) since this molecule quantitatively

reacts with the photogenerated superoxide. The decrease of the absorption intensity of the NBT solution measures the amount of superoxide formed hence the reductive capability of the photocatalyst.

To monitor the oxidative ability of the various systems, the formation of $OH^{\bullet}$ radicals has been followed by spin trapping technique using DMPO (5,5-dimethyl-pyrroline N-oxide) as a spin trap (see S.I., Figure S4). In this case, the intensity of the EPR signal of the DMPO-$OH^{\bullet}$ adduct is proportional to the amount of photoformed $OH^{\bullet}$ radicals (Fig.9B).

In analogy with the results obtained irradiating the samples under vacuum, also in this case the visible light does not cause formation of ROS. As expected, the formation of ROS species was indeed observed irradiating the samples with UV-Visible light. Inspection of Fig. 9 indicates some main facts:

a) the high loading Ce10-ZT sample (10%) is practically inactive in the production of ROS in both cases (Fig. 9A and 9B);

b) the low loading materials with 1% and 0.5% (Ce1-ZT, Ce0.5-ZT) are less active than the pristine matrix in the production of superoxide (photoinduced reduction ability, Fig. 9A), but more active in the production of $OH^{\bullet}$ radicals (oxidative ability, Fig. 9B).

These results indicate, first of all, that an excess of Ce loading is detrimental to the photochemistry of zirconium titanate since it evidently contains a high amount of recombination centers canceling the reactivity of both electrons and holes. Secondly, a moderate loading of Ce attenuates the recombination allowing, similarly to what observed in the case of cerium doped zirconia, an increase of the hole activity with respect to the pristine matrix. In the attempt to understand these puzzling results, some considerations on the chemical and electronic features of the solid have to be proposed. As put into evidence by XPS, the as prepared solid contains abundant amounts of Ce^{3+} in the structure. This alteration of the valence state of the cation (trivalent instead of tetravalent) can be compensated, in principle, in two ways e.g. with the formation of a hole that, in oxides, can be

described as an $O^{-\bullet}$ representing a magnetic impurity, or leading to compensating defects as oxygen vacancies (V_O), with one vacancy compensating the introduction of two trivalent ions, as discussed in the computational part, see § 3.2. [60,61] The absence of relevant EPR evidence of stabilized holes in the as prepared Ce-doped $ZrTiO_4$ samples (see Fig. 8) indicates that the compensation mechanism involves the formation of oxygen vacancies as observed for instance in the case of the well-known Y-doped ZrO_2. The presence of point defects, which can act as recombination centers, is usually detrimental for the photoactivity of semiconducting oxides.[62]

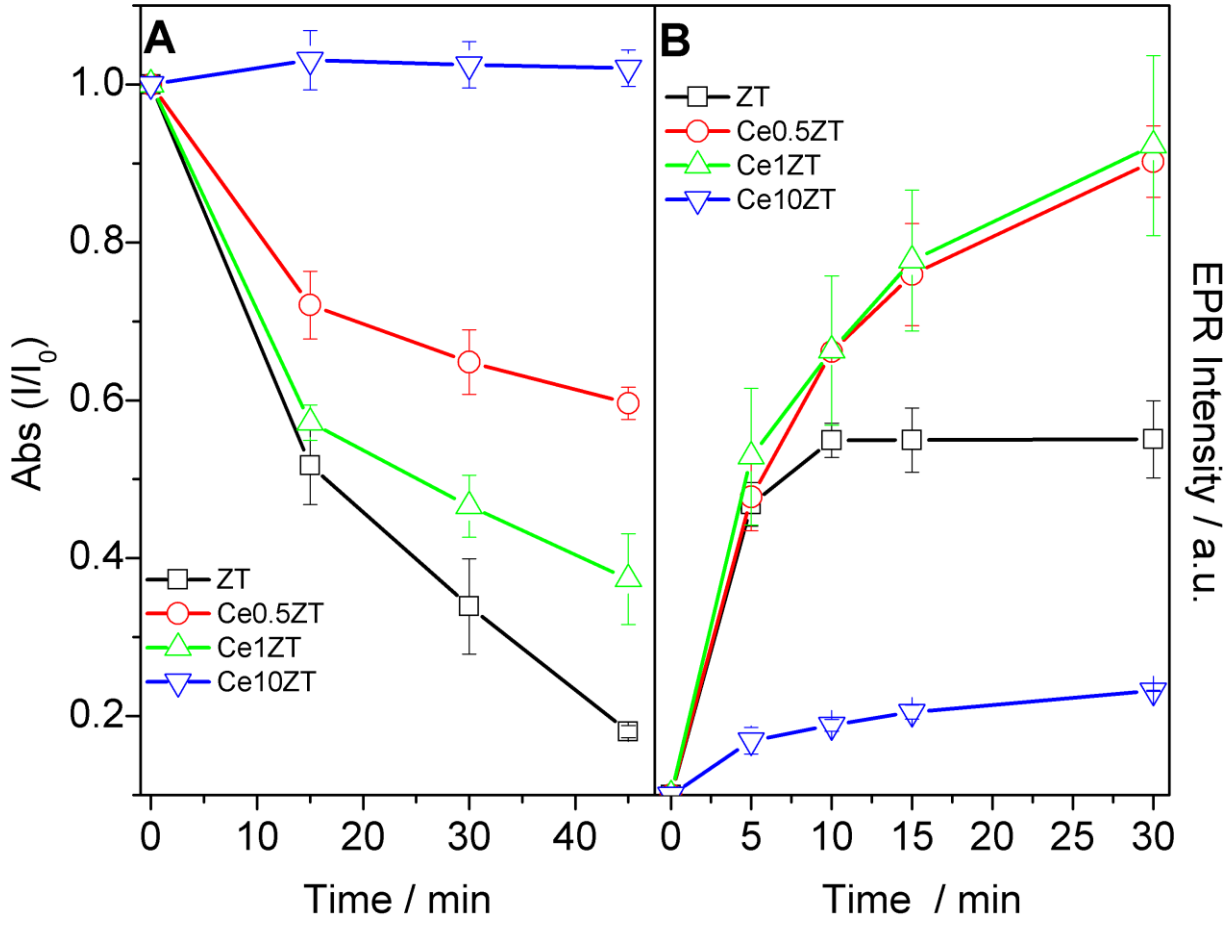

Figure 9: Panel A, Absorption intensity of NBT upon UV-Visible irradiation of different samples. Panel B, EPR intensity of the spectra of the DMPO/$OH^{\bullet}$ adduct produced by irradiation of a water suspension of different samples with UV-Visible light.

However, the insertion of Ce ions also causes the formation of intraband gap electronic states as described by our computational results. As mentioned in the introduction, the presence of empty

electronic states in the middle of the band gap due to a fraction of oxidized cerium ions (Ce^{4+}), on the contrary, can have a beneficial role on the photoactivity of an oxide.[31,32,33,34] In the present case the behavior of the analyzed samples is likely due to the delicate balance between the presence of Ce^{3+} (inducing the detrimental oxygen vacancies) and that of Ce^{4+} which can act as selective trapping sites for photoexcited electrons ($Ce^{4+} + e^- \rightarrow Ce^{3+}$) making the photogenerated holes more available for surface oxidation. In fact, the amount of oxygen vacancies (associated to the presence of Ce^{3+}) probably does not fully quench the photogenerated charge carriers and it is sufficiently low to allow the preferential trapping of the photoexcited electrons by the residual Ce^{4+}. Such preferential electron trapping inhibits the reductive capability of the material (results in Fig. 9A) and, at the same time, enhances the life time of the photogenerated holes, leading to a higher oxidizing capability in terms of $OH^{\bullet}$ radical production (Fig. 9B).

To summarise, the observed photoactivity is strictly related to the oxidation state of the cerium ions. In fact, for the Ce-doped ZrO_2 system, which show many physical-chemical features similar to that of Ce-doped $ZrTiO_4$, previous works published by some of us clearly shows that the presence of empty 4f states of the Ce(IV) is the key feature to improve the photoactivity, in particular with visible light[31,32,33]. In the Ce-doped $ZrTiO_4$ investigated here, the dominant Ce oxidation state is +3 (configuration [Xn] $4f^1$) and the response of the material to the both UV and Visible light is different. It is worth noting that also ZrO_2, when doped with a rare-earth element different from Ce (i.e. Erbium) with populated 4f states, the photoactivity is largely quenched.[34]

4. Concluding remarks

The data here reported indicate that the doping of $ZrTiO_4$ with cerium leads to a material that shows several features close to that of the homologous Ce-doped ZrO_2 system. In both cases a solid solution of cerium ions in the hosting oxide can be easily obtained and the doped material shows

an optical absorption extended to the visible range. Such absorption can be attributed to the presence of intra band gap states due to the Ce ions both in the reduced and oxidized form (Ce^{3+}/Ce^{4+}).

In spite of these close similarity, Ce-doped $ZrTiO_4$ differs from Ce-ZrO_2 in terms of response to both the UV and visible light. The visible light absorption in fact does not correspond to any relevant charge carrier separation and ROS generation. This suggests that in the case of $ZrTiO_4$ the charge carrier recombination processes prevails on the excitation one. Much likely, such difference is related to the high amount of Ce(III) induced by the formation of lattice defects (O vacancies) that are detrimental for the photoactivity of the Ce-doped $ZrTiO_4$ samples. Irradiating the samples with UV-Visible light the photoactivity, is strictly dependent on the cerium loading. For low loading the oxidizing capability increases, whereas for high cerium loading the photoactivity decreases. The present work highlights also how the oxidation state of the dopant plays a crucial role in determining the final properties of a doped oxide.

Acknowledgments

The work has been supported by the Italian MIUR through the PRIN Project 2015K7FZLH SMARTNESS "Solar driven chemistry: new materials for photo– and electro–catalysis". The µ-XRFresults have been obtained with the equipment acquired by the “G. Scansetti” Interdepartmental Centre for Studies on Asbestos and Other Toxic Particulates, thanks to a grant by the Compagnia di San Paolo, Torino, Italy.

References

[1] D. F. Ollis, E. Pelizzetti, N. Serpone, Env. Sci. Tech. 25 (1991) 1522-1529.

[2] S. Sakthievel, B. Neppolian, M.V. Shankar, B. Arabindoo, M. Palanichamy, V. Murugesan, Sol. Energy Mater. Sol. Cells 77 (2003) 65-82.

[3] E. Borgarello, J. Kiwi, E. Pelizzetti, M. Visca, M. Grätzel, Nature 289 (1981) 158-160.

[4] X. Chen, C. Li, M. Grätzel, R. Kostecki, S.S. Mao, Chem. Soc. Rev. 41 (2012) 7909-7937.

[5] M. Minella, V. Maurino, C. Minero, E. Pelizzetti, J. Nanosci. Nanotechnol. 15 (2015) 3348-3358.

[6] T. Hisatomi, J. Kubota, K. Domen, Chem. Soc. Rev. 43 (2014) 7520-7535.

[7] A. Fujishima, K. Honda, Nature 238 (1972) 37-38.

[8] F. Zhang, J. Zhao, T. Shen, H. Hikada, E. Pelizzetti, N. Serpone Appl. Catal. B Environmental 15 (1999) 147-156.

[9] J. Low, C. Jiang, B. Cheng, S. Wageh, A. A. Al-Ghamdi, J. Yu, Small Methods. 1, (2017) 1700080.

[10] M.A. Anderson, Surf. Sci. Rep. 66 (2011) 185-297.

[11] A. Kubacka, G. Colón, M. Fernández-García, Catal Today 143 (2009) 286-292.

[12] F. Spadavecchia, G. Cappelletti, S. Ardizzone, M. Ceotto, L. Falciola, J. Phys. Chem. C 115 (2011) 6381-6391.

[13] S. Rajendran, M.M. Khan, F. Gracia, J. Qin, V.K. Gupta, S. Arumainathan, Sci. Rep. 6 (2016) 31641

[14] Z. Xiu, Z. Xing, Z. Li, X. Wu, X. Yan, M. Hu, Y. Cao, S. Yang, W. Zhou, Mater. Res. Bull. 100 (2018) 191-197.

[15] X.-L. Luo, C.-J. Liu, M.-J. Chen, S.-S. Zhang, Y.-H. Xu, Mater. Res. Bull. 94 (2017) 428-434.

[16] N.S. Arul, D. Mangalaraj, R. Ramachandran, A.N. Grace, J.I. Han, J. Mat. Chem. A 3 (2015) 15248-15258.

[17] E. Garcia-Lopez, G. Marcì, F.R. Pomilla, M.C. Paganini, E. Giamello, L. Palmisano, Catal. Today 313 (2018) 100-105.

[18] F. Galindo, R. Gomez, M. Aguilar, J. Mol. Catal. A: Chem. 281 (2008) 119-125.

[19] S. Watanabe, X. Ma, C. Song, J. Phys. Chem C. 113 (2009) 14249-14257.

[20] J. Santiago-Morales, A. Aguera, M. Gomez, A. R. Fernandez-Alba, J. Gimenez, S. Esplugas, R. Rosal, App. Catal. B 129 (2013) 13-29.

[21] A. Makdee, P. Unwiset, K. C. Chanapattharapol, P. Kidkhunthod, Mater. Chem. Phys. 213 (2018) 431-443.

[22] C. Gionco, M. C. Paganini, S. Agnoli, A. E. Reeder, E. Giamello, J. Mater. Chem. A 1 (2009), 10918-10926.

[23] B.S. Liu, X.J. Zhao, N.Z. Zhang, Q.N. Zhao, X. He, J.Y. Feng, Surf. Sci. 595 (2005) 203-2011.

[24] J. Fang, X. Bi, D. Si, Z. Jiang, W. Huang, Appl. Surf. Sci. 253 (2007) 8952-8961.

[25] Y.H. Xu, H.R. Chen, Z.X. Zeng, B. Lei, Appl. Surf. Sci. 252 (2006) 8565-8570.

[26] T.Z. Tong, J.L. Zhang, B.Z. Tian, F. Chen, D.N. He, M. Anpo, J. Colloid Interf. Sci. 315 (2007) 382-388.

[27] P. Calza, C. Gionco, M. Giletta, M. Kalaboka, V.A. Sakkas, T. Albanis, M.C. Paganini, J. Hazard. Meter. 323 (2017) 471-477.

[28] M. Yashima, T. Hirose, S. Katano, Y. Suzuki, M. Kakihama, M. Yoshimura, Phys. Rev. B 13 (1995) 8018-8025.

[29] A.V. Emeline, V.N. Kuznetsov, V.K. Ryabchuk, N. Serpone, Environ. Sci. Pollut Res. 19 (2012) 3666-3675.

[30] N. Serpone, A.V. Emeline, J. Phys. Chem. Lett. 3 (2012) 673-677.

[31] C. Gionco, M. C. Paganini, E. Giamello, R. Burgess, C. Di Valentin, G. Pacchioni, J. Phys. Chem. Lett. 5 (2014) 447-451.

[32] M.C. Paganini, C. Gionco, E. Giamello, O. Sacco, V. Vaiano, D. Sannino, Adv. Sci. Lett. 23 (2017) 5906-5908.

[33] C. Gionco, M. C. Paganini, M. Chiesa, S. Maurelli, S. Livraghi, E. Giamello, Catal. Today 504 (2015) 338-343.

[34] C. Gionco, M. C. Paganini, E. Giamello, O. Sacco, V. Vaiano, D. Sannino, J. Energy Chem. 26 (2017) 270-276.

[35] S. Pol, V. Pol, A. Gedanken, G. Spijksma, J. Grinblat, R. K. Selvan, V. Kessler, G. Seisenbaeva, S. Gohil, J. Phys. Chem. C 111 (2007) 2484-2489.

[36] D-S. Kim, D.-H. Park, G.-D. Kim and S.-Y. Choi, Met. Mater. Int. 10 (2004) 361-365.

[37] P. Lessing, Z. Yang, G. Miller, H. Yamada, J. Electrochem. Soc. 135 (1988) 1049-1057.

[38] Y. Park, Phys. Rev. B 62 (2000) 8794-8801.

[39] R.E. Newnham, J. Am. Ceram. Soc. 50 (1967) 216-216.

[40] V. Polliotto, E. Albanese, S. Livraghi, P. Indyka, Z. Sojka, G. Pacchioni, E. Giamello, J. Phys. Chem. C 121 (2017) 5487-5497.

[41] V. Polliotto, E. Albanese, S. Livraghi, G. Pacchioni, E. Giamello, J. Mater. Chem. A 5 (2017) 13062–13071.

[42] L. Lutterotti, S. Matthies, H. R. Wenk, A. S. Schultz and J. W. Richardson, J. Appl. Phys. 81 (1997) 594-600.

[43] http://maud.radiographema.com

[44] A. D. Becke, J. Chem. Phys. 98 (1993) 5648-5653.

[45] C. Lee, W. Yang, R.G. Parr, Phys. Rev. B 37 (1988) 785-789.

[46] R. Dovesi, R. Orlando, A. Erba, C. M. Zicovich-Wilson, B. Civalleri, S. Casassa, L. Maschio, M. Ferrabone, M. De La Pierre, P. D'Arco, Y. Noël, M. Causà, M. Rérat, B. Kirtman. Int. J. Quantum Chem. 114, (2014) 1287-1317.

[47] P.J. Hay, W.R. Wadt, J. Chem. Phys. 82 (1985) 299-310.

[48] M. Dolg, H. Stoll, H. Preuss, J. Chem. Phys. 90 (1989) 1730-1734.

[49] J. Graciani, A.M. Márquez, J.J. Plata, Y. Ortega, N.C. Hernández, A. Meyer, C.M. Zicovich-Wilson, J. F. Sanz J. Chem. Theory Comput. 7 (2011) 56–65.

[50] J. Wang, J. Sun, Q. Jing, B. Liu, H. Zhang, Y. Yu, J. Yuan, S. Dong, X. Zhou, X. Cao, J. Eur. Ceram. Soc. 38 (2018) 2841-2850.

[51] P. Burroughs, A. Hamnet, A.F. Orchard, G. Thornton, J. Chem. Soc. Dalton Trans. 0 (1976) 1686-1698.

[52] A. Fujimori, Phys. Rev. B 28 (1983) 2281-2283.

[53] L. Artiglia, S. Agnoli, M. C. Paganini, M. Cattelan, G. Granozzi, ACS Appl. Mater. Interfaces. 6 (2014) 20130-20136.

[54] B. M. Reddy, A. Khan, Y. Yamada, T. Kobayashi, S. Loridant, J.-C. Volta J. Phys. Chem. B 107 (2003) 11475-11484.

[55] J. Graciani, J. J. Plata, J. F. Sanz, P. Liu and J. A. Rodriguez, J. Chem. Phys. 132 (2010) 104703.

[56] S. Agnoli, A. E. Reeder, S. D. Senanayake, Jan Hrbek, J. A. Rodriguez, Nanoscale 6 (2014) 800–810.

[57] Gallino, F.; Pacchioni, G.; Di Valentin, C. J. Chem. Phys. 133 (2010) 144512.

[58] F. Oba, A. Togo, I. Tanaka, J. Paier, G. Kresse, Phys. Rev. B 77 (2008) 245202.

[59] C. Minero, G. Mariella, V. Maurino, E. Pelizzetti, Langnuir 16 (2000) 2632-2641.

[60] A. R. West, Solid State Chemistry and its Applications, 2nd edition. John Wiley & Sons, Ltd.: 2013.

[61] C. Gionco, S. Livraghi, S. Maurelli, E. Giamello, S. Tosoni, C. Di Valentin, G. Pacchioni, Chem. Mater. 27 (2015) 3936-3945.

[62] O. Carp, C.L. Huisman, A, Reller, Prog. Solid State Chem. 32 (2004), 33-117.